Ultrafast Photoinduced Heat Generation by Plasmonic HfN Nanoparticles

Devin B. O'Neill, Sean K. Frehan, Kaijian Zhu, Erwin Zoethout, Guido Mul, Erik C. Garnett,* Annemarie Huijser, and Sven H. C. Askes

There is great interest in the development of alternatives to noble metals for plasmonic nanostructures. Transition metal nitrides are promising due to their robust refractory properties. However, the photophysics of these nanostructures, particularly the hot carrier dynamics and photothermal response on ultrafast timescales, are not well understood. This limits their implementation in applications such as photothermal catalysis or solar thermophotovoltaics. In this study, the light-induced relaxation processes in water-dispersed HfN nanoparticles are, for the first time, elucidated by fs transient absorption, Lumerical FDTD and COMSOL Multiphysics simulations, and temperature-dependent ellipsometry. It is unequivocally demonstrated that HfN nanoparticles convert absorbed photons into heat within <100 fs; no signature of hot charge carriers is observed. Interestingly, under high photon energy or intense irradiation stimulated Raman scattering characteristic of oxynitride surface termination is observed. These findings suggest that transition metal nitrides could offer benefits over noble metals in the field of plasmonic photothermal catalysis.

1. Introduction

Plasmonic nanostructures, especially those made from noble metals, attract widespread attention owing to their high and tunable optical cross section, light concentration effects, and hot carrier generation.[1,2] This has led to significant interest in plasmonic nanostructures for photocatalysis, either through local heat generation or as a photosensitizer.[3,4] Materials in the family of plasmonic transition metal nitrides (e.g., TiN,

HfN, NbN, WN) feature high thermomechanical robustness and recently have been proposed for applications requiring extreme operating conditions, such as photothermal catalysis or solar thermophotovoltaics.[5] These materials have high melting points and demonstrate high temperature durability, chemical stability, and corrosion resistance, while presenting an optical response similar to Au or Ag plasmonic nanostructures.[5,6] With a strong response in the visible range, high mechanical hardness, low material cost,[6–9] and outstanding performance in electrochemical reactions,[10–12] the photophysics of these materials requires further research. In the following, we will briefly review the current level of understanding of the photophysics of noble metal plasmonic particles, followed by a discussion on transition metal nitride plasmonic nanoparticles.

Light absorption and heat generation by noble metal nanoparticles can be summarized as follows: first, the local surface plasmon resonance (LSPR) is excited, which lasts several fs and decays by nonradiative dephasing through Landau damping (1–100 fs). This process generates hot carriers at regions with high optical absorption (hotspots), the hot carriers subsequently decay by electron–electron scattering (1–100 fs) followed by electron–phonon coupling (0.1–10 ps). Ultimately, phonons dissipate heat to the surroundings (1–10 ns).[4,13,14] There is increasing interest in hot carrier processes, chemical reactions induced by them, and determining whether the observed changes in chemical reactions are due to lattice heating or hot charge carriers.[15,16]

Since elementary chemical transformations typically occur on a 1–100 ps timescale,[17] it is essential to characterize the light-induced carrier dynamics and thermal relaxation of plasmonic systems that consist of non-noble metal materials. Recent studies have shown that in particular hafnium nitride (HfN) performs well at converting light into heat through thermoplasmonic relaxation.[18,19] This efficient light-induced heating likely stems from a less negative real permittivity (ε') and a higher imaginary permittivity (ε'') of HfN relative to noble metals, leading to a lossy plasmonic response accompanied by lower electric field magnification,[20–24] fast plasmonic dephasing, spectral broadening of the LSPR,[4] and, most importantly, high optical absorption. Overall, these properties are highly attractive

D. B. O'Neill, S. K. Frehan, K. Zhu, Prof. G. Mul, Dr. A. Huijser
PhotoCatalytic Synthesis Group
MESA+ Institute for Nanotechnology
University of Twente
P.O. Box 217, Enschede 7500 AE, The Netherlands
Dr. E. Zoethout
Dutch Institute for Fundamental Energy Research (DIFFER)
De Zaale 20, Eindhoven 5612 AJ, Netherlands
Prof. E. C. Garnett, Dr. S. H. C. Askes
Center for Nanophotonics
NWO Institute AMOLF
Science Park 104, Amsterdam 1098 XG, The Netherlands
E-mail: E.Garnett@amolf.nl

ADVANCED
SCIENCE NEWS
www.advancedsciencenews.com

ADVANCED
OPTICAL
MATERIALS
www.advopticalmat.de

for plasmonic heat generation with broadband light sources, such as in photothermal catalysis or photothermal therapy,[25,26] or Raman applications where material robustness and resistance to thermal deformation is required.[27,28]

Presently, the photodynamics of HfN is not well understood, with a discrepancy in the literature. On the one hand, experimental work on HfN thin films has ascribed a long-lived (ns) signal to the slow decay of hot carriers,[29–33] whereas on the other hand, theoretical work has predicted a maximum hot carrier lifetime of only 10 fs.[34] Furthermore, the understanding of TiN and ZrN thin-film photodynamics has shifted recently from long-lived carriers to the present understanding of very strong electron-phonon coupling with the use of fs spectroscopy.[34–38] Thus, further research is required to resolve this discrepancy and elucidate the hot carrier dynamics and photothermal temporal response of plasmonic HfN nanoparticles.

In this work, we investigate the photophysical relaxation processes in water-dispersed HfN nanoparticles using fs transient absorption (TA) spectroscopy. By combining the TA results with optical simulations and an advanced 3D two-temperature model, it is unequivocally demonstrated that the photodynamics of HfN nanoparticles are characterized by an ultrashort hot carrier lifetime and concomitant ultrafast lattice heating. Furthermore, by using optical constants from temperature-dependent ellipsometry experiments we show that the observed transient spectral features could be faithfully reproduced by only implementing this thermal effect. Interestingly, under particular photoexcitation conditions a signature of stimulated Raman scattering at early times (≈100 fs) is observed, indicative of a photochemical surface reaction. Finally, given our experimental and numerical results, we hypothesize that the dominant mechanism for HfN in photochemical applications should be almost purely thermal (lattice heating), making it a useful system for mechanistic studies.

2. Results and Discussion

The HfN nanoparticles form a purple, transparent, colloidal suspension of well-dispersed particles in water (**Figure 1**a), with a clear plasmonic UV–Vis absorption band centered at 555 nm and an inter-band transition in the UV region. The asymmetry and relative broadness of the plasmonic band is indicative of the effect of the size and shape distribution.[39] The X-ray diffraction pattern (Figure 1b) shows the narrow peaks of cubic rock-salt crystalline HfN,[40] with a minor impurity of unreacted HfO_2 precursor. Since HfO_2 has no optical absorption in the visible range, no further purification is necessary.[41] Scanning electron microscopy (SEM) images show near-spherical particles with an average diameter of 18 nm (Figure 1c,d), while 90% of the particles have an ellipsoid aspect ratio below 1.5. Energy-dispersive X-ray spectroscopy (EDS) of single particles confirm the Hf and N constituents and additionally show the signature of a self-passivating oxide or oxynitride shell around the particles (Figure 1e–g).[42–44] Overall, the HfN nanoparticles are of high quality and suitable for TA experiments.
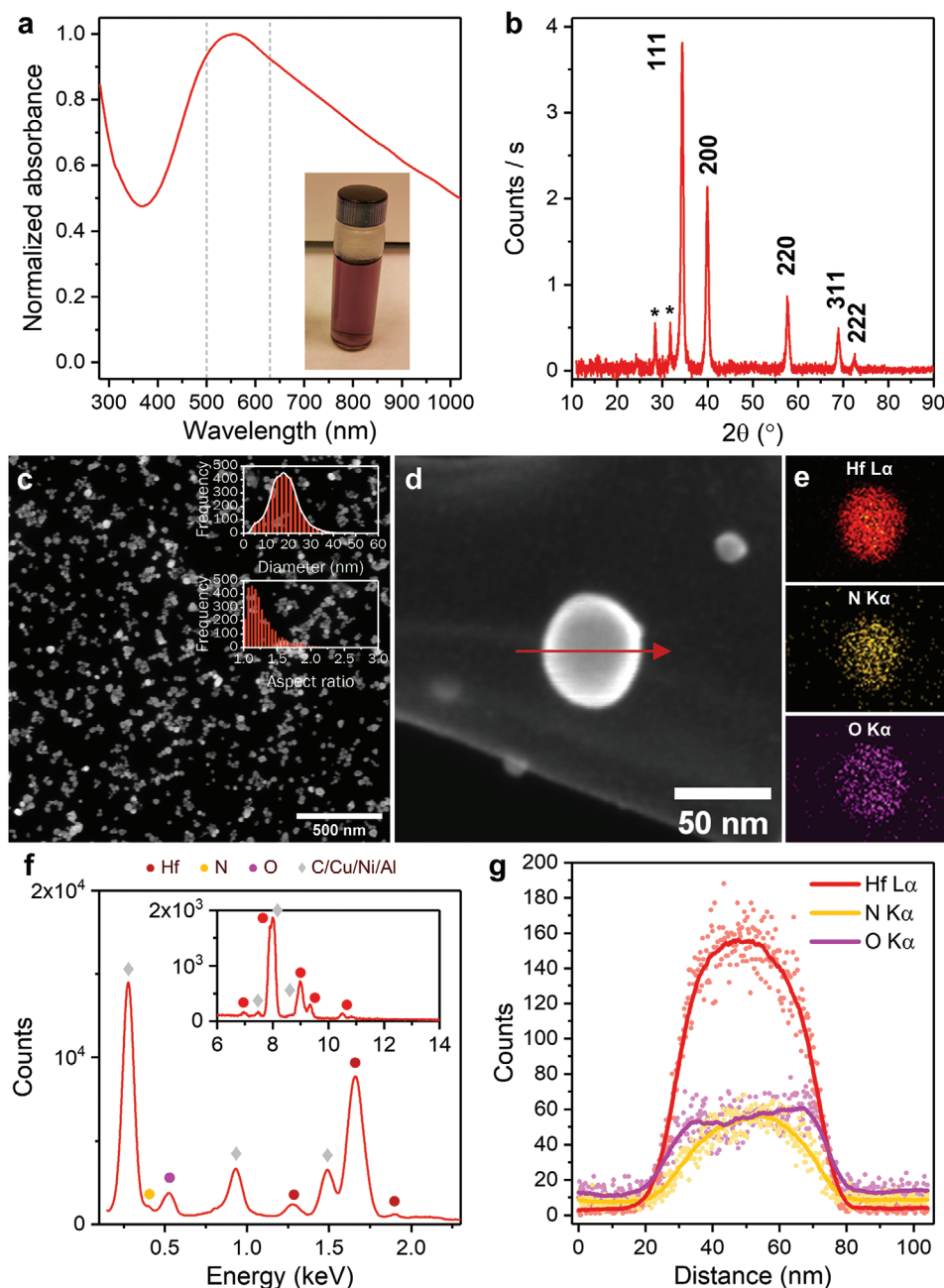
Figure 2 shows the TA data of the HfN nanoparticles dispersed in water, recorded at 500 nm excitation (for data at 630 nm excitation, see Figure S1 in the Supporting

Information). We attribute the decrease in absorbance around 475 nm to attenuated LSPR absorption, while the positive signal $\lambda < 400$ nm is likely due to LSPR broadening.[47] The TA spectrum shape is constant at all time delays (Figure S2, Supporting Information) showing little significant change in spectral shape in time; while the TA signal decays in several hundred ps. Changing the excitation wavelength from 500 nm to 630 nm shows no significant change in TA spectrum (Figure S3, Supporting Information). At this point, it is important to realize that both light-induced changes in energy distribution of the charge carriers and lattice temperature contribute to the transient signals, with the electronic component typically being more pronounced than that arising from heat dissipation.[48] On the one hand, photoexcitation causes a change in energy distribution of the charge carriers, with less electrons at the Fermi level to contribute to the plasmon dipole, thereby attenuating and broadening the LSPR band. In a TA spectrum, this effect typically induces a loss of absorption around the LSPR wavelength (bleach) and gain in absorption at either side, which is typically referred to as "wings" (the lack of a positive wing at lower energies is attributed to the width of the HfN LSPR band, with the low energy wing being expected into the NIR).[47] On the other hand, the subsequent electron–electron scattering and electron–phonon coupling lead to thermal expansion of the lattice lowering the effective carrier concentration and metallicity (ε'), while the increasing phonon population and electron–phonon interactions result in higher losses (higher ε''). As a result, an elevated lattice temperature also produces a lower quality LSPR and broadens the absorption band, similar but not identical to electronic effects.[47–50] As the difference in relative intensities of electronic and thermal effects normally results in a multi-exponential decay in time,[47] and here only a single decay is observed; therefore, the observed spectral response cannot be unambiguously assigned to an electronic or thermal effect.

When comparing the temporal response of HfN nanoparticles with Au nanoparticles as a well-studied benchmark, both dispersed in water (top panels Figure 2), a notable difference is evident. The TA decay of Au nanoparticles is well described by a two-component exponential decay ($\tau_1 = 4.6 \pm 0.1$ ps, $\tau_2 = 65 \pm 4$ ps, Figure S4a, Supporting Information), for which the typical lifetime of hot electrons (τ_1) can be clearly distinguished[51] followed by thermal dissipation (τ_2). In contrast, the TA signal of the HfN nanoparticles decays in what appears to be a single process with no evidence of a two-component exponential decay. Since the observed decay roughly coincides with the time-regime of thermal dissipation in plasmonic systems (0.1–10 ns), we tentatively fit a stretched exponential function that is characteristic for this phenomenon[49] to the decay traces:
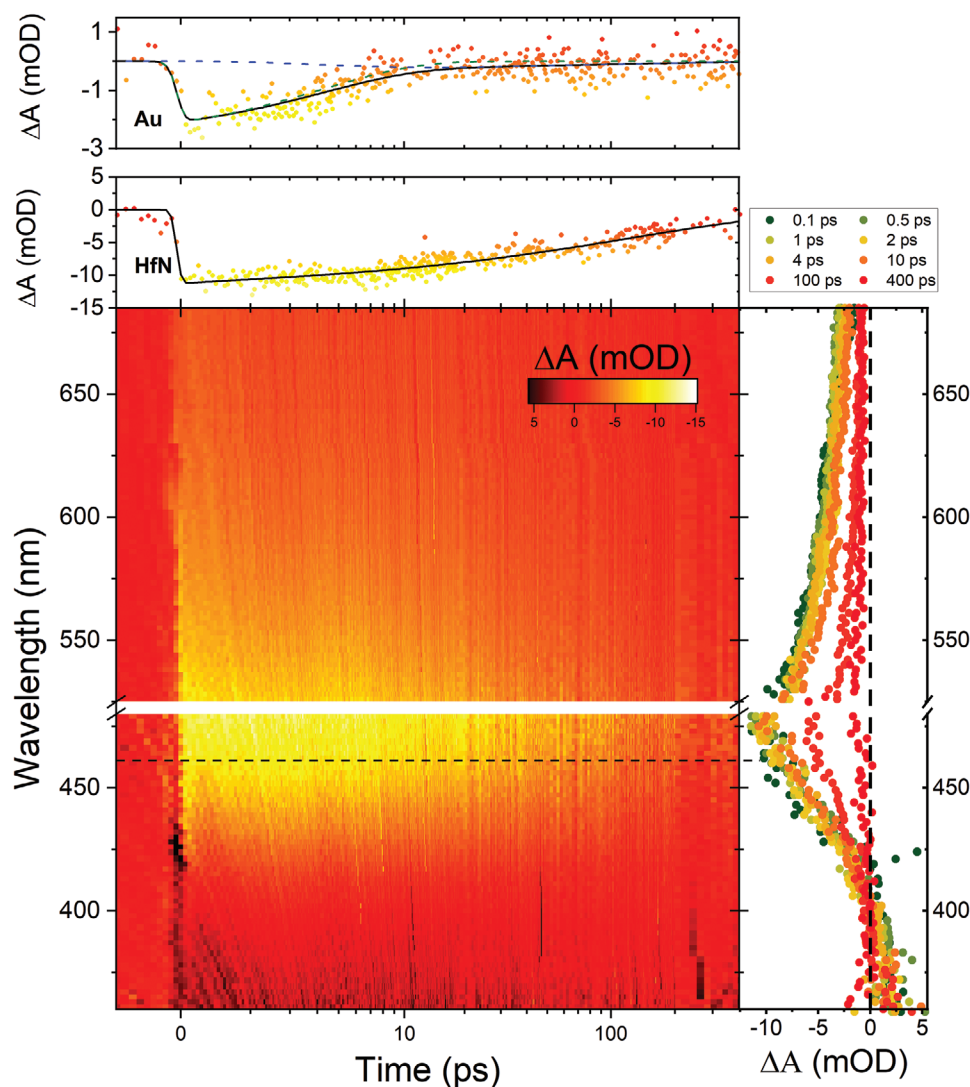
$$f(t) = Ae^{-(t/\tau)^\beta} \text{erf}(t/w) \tag{1}$$

where β modifies the rate of decay (reported as $\beta \approx 0.6$-0.7 for 15–50 nm diameter spherical Au nanoparticles),[49] which is governed by the time constant τ, and the signal rise-time is modeled by an integrated Gaussian with width w, also known as an error function. While β is allowed to vary between 0.1 and 1 during the fitting, it converges to 0.5 ± 0.1 for both 500 and 630 nm excitation with excellent agreement at both short and long timescales. The decay time is found to be similar

**ADVANCED
SCIENCE NEWS**
www.advancedsciencenews.com

**ADVANCED
OPTICAL
MATERIALS**
www.advopticalmat.de

Figure 1. Physical and optical characterization of HfN nanoparticles. a) Normalized UV–Vis absorption spectrum with inset photograph of the nanoparticles in water. The photoexcitation wavelengths used in this work are indicated with dashed lines. b) X-ray diffraction pattern with indexed HfN peaks.[45,46] Asterisks (*) indicate HfO_2 peaks (COD card 400-1331). c,d) Scanning electron micrographs. Particle size distribution and ellipsoid-fitted aspect-ratio distribution of 3420 analyzed nanoparticles shown as insets in panel (c). e) Energy dispersive X-ray (EDX) analysis of the particle shown in panel (d). f) EDX spectrum of the particle shown in panel (d). Signals of the support grid and microscope indicated by grey diamonds. Inset shows the higher-energy region. g) EDX line scan of the particle in (d), along the red arrow. Moving average lines are added to guide the eye. Note that the relative intensities of signals are not calibrated to reflect the atomic composition.

for the two photoexcitation wavelengths: $\tau_{500\,nm} = 130 \pm 10$ ps, and $\tau_{630\,nm} = 120 \pm 20$ ps. We have explored several other fitting functions to scrutinize the temporal decay as well. Fitting with a single-component exponential gives a discrepancy at longer time scales (Figure S5, Supporting Information). A two-component exponential function affords a reasonable fit

to the data, but both decay-associated spectra are virtually identical (Figure S6, Supporting Information). This is also evident from the absence in spectral evolution in time (Figure 2), thus no transition from a hot electron regime to a thermal regime is observed. Overall, our TA data exclusively show signals of thermal dissipation in the HfN nanoparticles, with no sign of

ADVANCED
SCIENCE NEWS
www.advancedsciencenews.com

ADVANCED
OPTICAL
MATERIALS
www.advopticalmat.de

Figure 2. TA contour plot with λ_{exc} = 500 nm for HfN nanoparticles in water. Right: spectra at selected time delays. Top: time-trace of Au nanoparticles in water probed at 524 nm, with a two-component exponential fit (τ_1 = 4.6 ± 0.1 ps, τ_2 = 65 ± 4 ps). Middle: time-trace for HfN nanoparticles in water probed at 462 nm, with a stretched-exponential fit (Equation (1), see text).

hot charge carrier decay, for which we present further evidence based on simulations below.

The normalized decay associated spectra (Figure S3, Supporting Information) show little change with excitation wavelength (500 nm and 630 nm); interestingly, with the center wavelength for the bleach being some 80 nm blue-shifted from the center of the plasmonic band (in contrast to gold, where the bleach is centered on the plasmon band).[47] While there is normally a short-lived blue-shift in plasmonic particles after excitation owing to excited electrons,[52] this is not the case here as the blue-shift is retained throughout the observed time frame. Accordingly, this blue shift most likely arises from the lattice temperature, which likely also causes a blue shift in the plasmon resonance.[53]
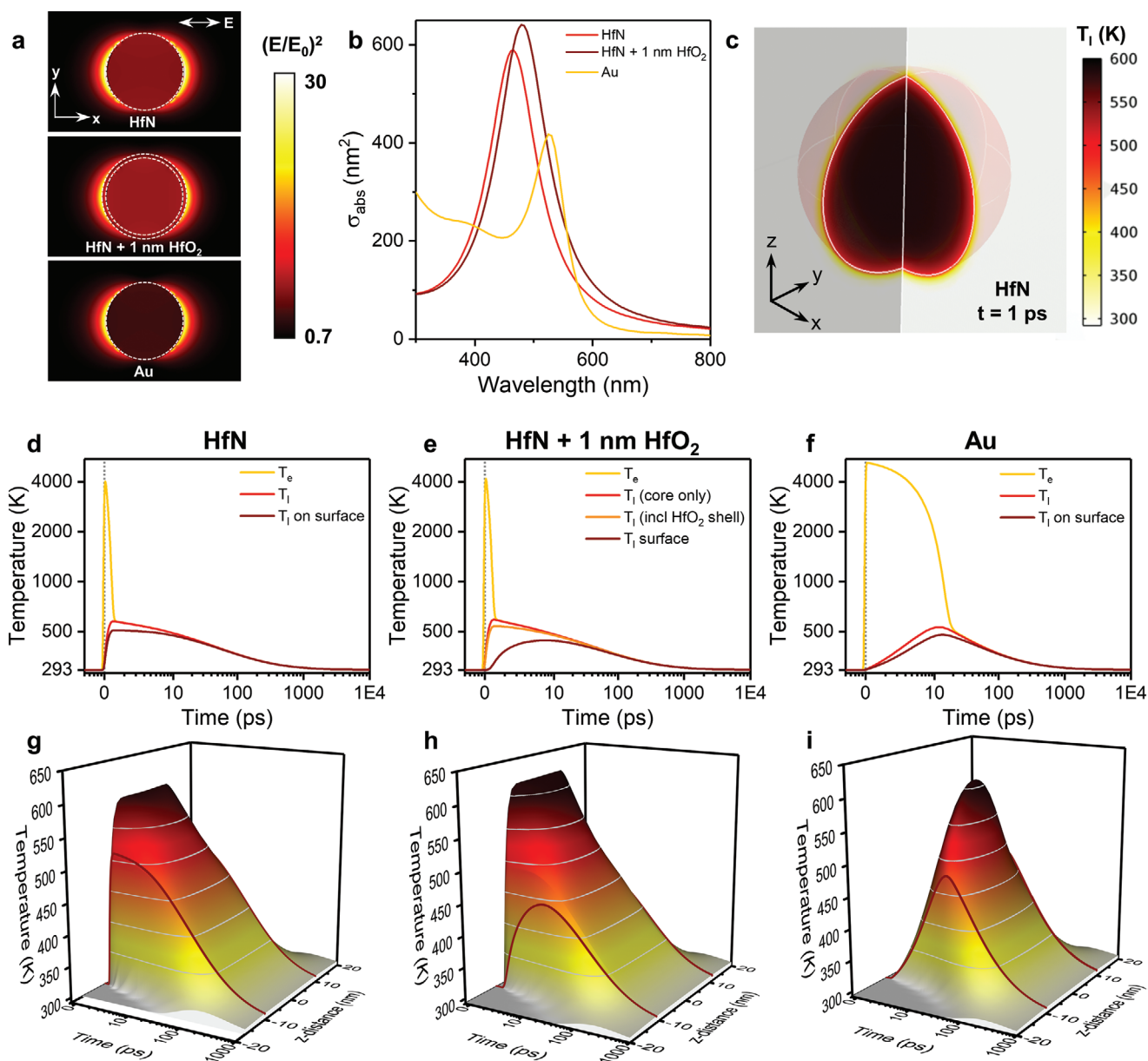
The absence of a signature of hot carrier decay in the TA data strongly suggests that electron–phonon coupling occurs at the same timescale or faster than our temporal resolution of ≈100 fs. To corroborate this implication, we have calculated the electron–phonon coupling constant (G in W/m^3 K) from literature data using Equation (2):[36,38,54]

$$G = \frac{3\gamma\lambda\langle\omega_2\rangle\rho}{\hbar\pi k_B M_W} \qquad (2)$$

where γ is the Sommerfeld constant, λ is the Bardeen-Cooper-Schrieffer electron–phonon coupling constant, $\langle\omega_2\rangle$ is the second moment of the phonon spectrum, ρ is the material density, $\hbar$ is the reduced Planck's constant, k_B is the Boltzmann constant and M_W is the molar weight of HfN. Although $\langle\omega_2\rangle$ is not well known for HfN, it could be estimated from the Debye temperature θ_D. This results in calculated electron–phonon coupling constants of 1.4×10^{18} W/m^3 K for HfN, and 2.8×10^{16} W/m^3 K for Au (see Table S2, Supporting Information and associated text for more details).[36,55–59] Thus, the electron–phonon coupling in HfN is roughly 50 times stronger than in Au, which directly implies a significantly faster hot electron

ADVANCED
SCIENCE NEWS
www.advancedsciencenews.com

ADVANCED
OPTICAL
MATERIALS
www.advopticalmat.de

Figure 3. Time-dependent simulation results modeling the evolution and dissipation of heat from 20 nm diameter HfN and Au nanoparticles upon 50 fs photoexcitation (3.2 W cm^{-2}). a,b) Electric field intensity cross sections (a) and absorption cross section spectra (b) simulated by Lumerical FDTD. c) Modeling of heat dissipation: a render of the heat distribution 1 ps after a pulse illuminates a HfN particle. d–f) Average temperature of the electrons (T_e) and lattice (T_l) in time for a HfN nanoparticle without (d) and with a 1 nm oxide layer (e), and for an Au nanoparticle (f). g–i) Temporal lattice temperature profiles along the z-axis of the spheres. The surface temperature is shown as dark-red lines. For panels (d)–(i), the heat pulse is centered at 0 ps. An animation of the 3D heat dissipation is given in Video S1, Supporting Information.

decay. Accordingly, with a hot electron–phonon coupling time $\tau_1 = 4.6 \pm 0.1$ ps for Au nanoparticles, the estimated time constant for HfN is on the order of 100 fs, close to the instrumental temporal resolution. As a result, hot electron decay is not resolved, and the TA decay almost certainly originates from thermal dissipation only.

To further explore the photophysical dynamics of the HfN nanoparticles, finite difference time domain (FDTD) simulations have been combined with an advanced 3D two-temperature model to simulate the energy flow in the system, fully accounting for thermal conduction of both electrons and phonons (see Supporting Information for details). These simulations, based on thin-film optical constants of HfN[39] and Au, show that 20 nm diameter HfN and Au nanoparticles have similar dipole electric field enhancements (**Figure 3**a), with a higher internal electric field for HfN nanoparticles. We additionally consider the case where the HfN particle is covered with a thin 1 nm HfO$_2$ shell, based on previously measured X-ray photoelectron spectroscopy depth profiles and Rutherford backscatter spectroscopy results of HfN thin films,[39] which red-shifts the

ADVANCED
SCIENCE NEWS
www.advancedsciencenews.com

ADVANCED
OPTICAL
MATERIALS
www.advopticalmat.de

LSPR slightly. Since the absorbed power is proportional to the product of the square of the electric field and the imaginary permittivity, both HfN nanoparticles have a larger absorption cross section than an Au nanoparticle (Figure 3b). When accounting for the observed size and shape polydispersity of the HfN nanoparticles (Figure S11, Supporting Information), the same conclusions uphold: the HfN nanoparticles in this work consistently absorb more light than their Au counterparts, especially at the pump wavelengths. Hence, we regarded the 20 nm diameter spherical model as representative for the synthesized HfN solution. The spatial absorbed power map is used as laser heating term ($q(x,y,z,t)$) in the two-temperature model. This model is governed by Equations (3) and (4):

$$C_e\left(T_e\right)\frac{\partial T_e}{\partial t} = \nabla\left[\kappa_e\left(T_e\right)\nabla T_e\right] - G\left(T_e - T_l\right) + q\left(x,y,z,t\right) \qquad (3)$$

$$C_l\left(T_l\right)\frac{\partial T_l}{\partial t} = \nabla\left[\kappa_l\left(T_l\right)\nabla T_l\right] + G\left(T_e - T_l\right) \qquad (4)$$

where subscripts e and l distinguish between electronic and lattice terms, T is the temperature (in K), $C(T)$ is the temperature-dependent volumetric heat capacity (in W/m³ K), $\kappa(T)$ is the temperature-dependent thermal conductivity (in W/m K), and G is the electron–phonon coupling constant that facilitates heat exchange between T_e and T_l. Although G is temperature-dependent as well,[60] from theoretical data on TiN and Au we estimate it to be roughly constant in the temperature range in this work.[38] These partial differential equations are solved with a finite element method in COMSOL Multiphysics, from which the spatial T_e and T_l time-profiles are extracted (Figure 3c-i).

The results of the simulations for both HfN and Au nanoparticles (Figure 3 and Video S1, Supporting Information) show the evolution of the electron and lattice temperatures in time following photoexcitation. Initially, the electron temperature rises, followed by a relaxation and transfer of energy to the lattice resulting in the lattice temperature increasing, which finally equilibrates with the surrounding water (Figure 3c-i). Both HfN and Au nanoparticles show comparable electron temperatures after photoexcitation (centered at 1 ps). However, whereas in Au nanoparticles the hot electrons are fully thermalized after 10 ps, this process occurs much more rapidly in HfN, in about 250 fs. Simultaneously, the HfN lattice heats up almost uniformly to ≈600 K with the onset of a large temperature-gradient across the metal-water interface (Figure 3d,g). Meanwhile, the Au nanoparticle reaches a lower temperature due to the lower absorbed power. Note that these peak temperatures are much higher than what is achieved for individual particles by continuous wave illumination at the same intensity ($\Delta T \approx 0.2$ mK, see Section S2.3, Supporting Information). The inclusion of the thermally isolating HfO$_2$ thin shell ($\kappa_{HfO_2} \approx 1.1$ W/m K) decreases the maximum surface temperature drastically (Figure 3e,h). Note, however, that in practice the shell will be an oxynitride material (HfO$_x$N$_y$, or heavily N-doped HfO$_2$) and will be expected to have a higher thermal conductivity than pristine HfO$_2$[61] and may also contribute to plasmonic behavior and absorption; that is, the presented data can be considered as a lower-limit case for the surface temperature response. When examining the

thermal dissipation after the electron–phonon coupling regime (>10 ps), the HfN nanoparticle dissipates the heat while maintaining a fairly uniform internal heat profile, while in the Au nanoparticle there is a larger heat gradient between core and surface on the 10–100 ps timescale (Figure 3f,i). This difference can be interpreted as the result of the lower heat capacity of Au than HfN (Figure S8, Supporting Information) and high gold/water interfacial thermal conductivity,[62,63] causing the surface to cool down quicker when in contact with H$_2$O. Eventually, each examined nanoparticle is fully cooled down to ambient temperature after several ns. Crucially, just as for the TA data, the simulated thermal dissipation can only be satisfactorily fitted using a stretched exponential decay (Equation 1, Figure S12, Supporting Information), and not with a single or double exponential function. Additionally, the simulated data for Au nanoparticles is in excellent agreement with both literature and our TA results (Figure 2). the calculated e-ph regime is on the order of 10 ps and thermal dissipation occurs over 100's ps,[47] comparably our TA result in $\tau_{e\text{-ph}} = 4.6 \pm 0.1$ ps and $\tau_{ph\text{-ph}} = 65 \pm 4$ ps. Accordingly, the simulations are accurate representations of the Au particle relaxation, and validate the simulations for HfN. Ultimately we conclude that the fs TA signal is exclusively due to thermal effects without electronic contribution.

Next, to explain the spectral shape of the TA data we have measured the influence of temperature on the optical constants by temperature-dependent ellipsometry. A high quality thin HfN[39] film was deposited on Si, protected from heat-induced oxidation by a 10 nm film of atomic-layer deposited (ALD) Al$_2$O$_3$, and the complex reflection has been measured on an ellipsometer fitted with a heating stage. The Al$_2$O$_3$ layer successfully protects the HfN from oxidizing and roughening during heating, with the retrieved spectra being unchanged before and after the cycle (Figure S14, Supporting Information). This is not the case for unprotected HfN (Figure S15, Supporting Information). The model-extracted optical constants of the HfN thin film from room temperature to 523 K are shown in **Figure 4a**,b. At elevated temperature, HfN has a less negative real permittivity and a higher imaginary permittivity, with changes being near-linearly dependent on temperature. At 450 nm, heating the sample to 523 K results in a 10% difference in both parameters. As recently explained in literature for TiN thin films,[64,65] these results can be interpreted by two physical effects upon heating. First, the lattice expands, which reduces the carrier concentration and the screened plasma frequency (where $\varepsilon' = 0$). Second, an elevated temperature increases the phonon population, which leads to an increase in phonon scattering and increased attenuation by the bulk material. Finally, we used the temperature-dependent optical constants to estimate the attenuation cross section spectrum (in nm²) from Mie Theory at each temperature during the simulated temperature decay of the HfN nanoparticle by Equation 5:[66]

$$\sigma_D\left(T_l,\lambda\right) = \frac{24\pi^2 r^3 \varepsilon_m^{\frac{3}{2}}}{\lambda} \times \frac{\varepsilon''\left(T_l,\lambda\right)}{\left(\varepsilon'\left(T_l,\lambda\right) + 2\varepsilon_m\right)^2 + \varepsilon''\left(T_l,\lambda\right)^2} \qquad (5)$$

where r is the particle radius (in nm), t is time, and ε_m is the permittivity of the aqueous medium (1.729). By subtracting
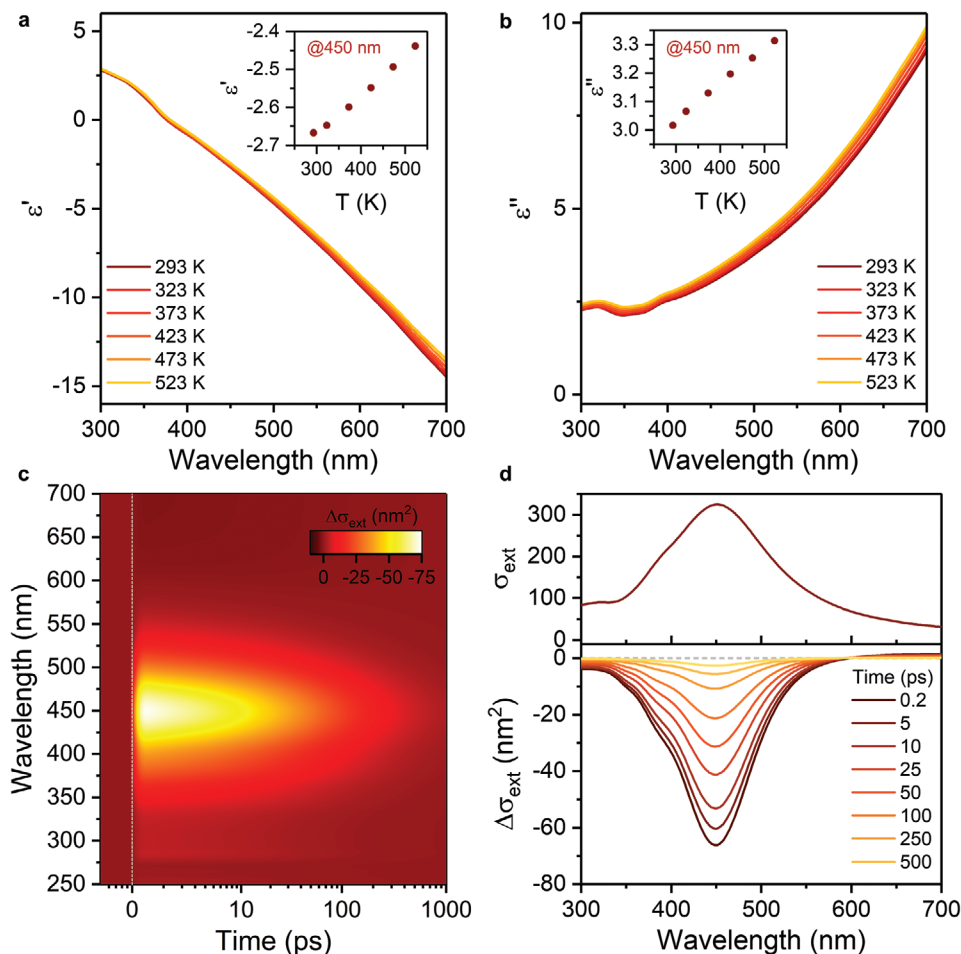
Figure 4. Temperature-dependent ellipsometry and simulated TA data. a) Real and b) imaginary permittivity of a 160 nm thin film HfN at 50 K intervals, up to 523 K. The insets show the near-linear response of each part as a function of temperature at $\lambda = 450$ nm. c,d) Simulated TA contour plot and spectra at selected time delays, generated from Mie Theory (Equation (5)).

the absorption cross section spectrum at 293 K, a fully simulated TA data set has been generated (Figure 4c,d). Due to the changes in optical constants, the LSPR band is bleached and broadened when the material is heated, with a change of about 25% when the particle reaches 600 K. The attenuated absorption is centered at the LSPR center wavelength at room temperature. We attribute small differences between experimental and simulated TA diagrams (spectral broadening, central LSPR wavelength) to the polydispersity of the experimental particles and the inherent differences between sputter-coated and solid-state synthesized HfN. Taken altogether, these data show that an elevated lattice temperature can fully account for the experimentally observed TA behavior of HfN nanoparticles.

The conclusions of this work are in strong contradiction with some recent literature that concluded hot carriers are responsible for the long transient signal observed in HfN thin films.[29–33] However, their analysis does not account for heat generation and dissipation, which is known to be significant in other transition metal nitrides.[37,59,67] It is clear from our analysis that heat has a profound influence on the transient optical response of HfN nanoparticles. Further, they concluded that a phonon-bottleneck is responsible for preventing phonon decay

and retaining a hot electron bath,[31] while not accounting for a defect-rich material which, much like our material, would not effectively support one. Conversely, the conclusion of ultrafast heat generation is in line with both observations and theoretical work for similar group-4 metal nitrides (TiN and ZrN).[9,36,37,65] Conclusively, given a real-world defect-rich material, we are confident that the origin of long-lived TA signals stem from thermal dissipation.

As our findings reveal an ultrashort hot charge carrier lifetime in HfN nanoparticles, with little to no opportunity to harvest thermalized carriers, the question is whether HfN's hot carriers can play a role in plasmonic photochemistry. On the one hand, not yet thermalized "ballistic" hot charge carriers could play an important role in photochemical enhancements observed in literature.[68] However, ballistic hot electrons in HfN have been calculated to have a shorter lifetime than in Au,[34] making it unlikely they can be harvested with respectable efficiency. The same likely applies to ballistic hot holes, although these have not yet been explored.[69] On the other hand, thermalized electrons can be harvested as well, albeit with lower energy than ballistic ones.[4] However, when transforming the simulated electronic temperature from Figure 3d to a thermalized

ADVANCED
SCIENCE NEWS
www.advancedsciencenews.com

ADVANCED
OPTICAL
MATERIALS
www.advopticalmat.de

Fermi-Dirac distribution (Figure S13, Supporting Information), the available thermalized electron energy in time is strikingly low for HfN, compared to Au: only during the laser pulse do the hot electrons and holes exceed 0.5 eV above and below the Fermi level, respectively. Conclusively, it is unlikely that HfN nanoparticles will prove to be a good hot carrier photocatalyst, but instead may be an excellent thermo-plasmonic material in which hot carrier effects are nearly abolished—as there has been much recent debate on disambiguating the role that hot carriers and local heat generation have in plasmon-driven processes.[15] In that respect, HfN is one of the most attractive material of the transition metal nitride family, as it combines the highest visible-range LSPR quality factor ($Q_{LSPR} = -\varepsilon'/\varepsilon''$),[70] together with ZrN, with the fastest heating: the electron–phonon coupling of HfN (1.4×10^{18} W/m^3 K) is higher than that of TiN or ZrN (0.8–1.0×10^{18} and 1.0×10^{18} W/m^3 K, respectively).[37] The ultrafast heating could be exploited in a number of applications, such as pulsed photothermal therapy and catalysis, photo-acoustic imaging, fast thermoelectronics, thermo-photovoltaics, and optical nanofabrication with sub-wavelength resolution.

While electron–phonon coupling is not observed in TA, likely since it occurs within the instrumental response time, an interesting phenomenon is observed at early times (**Figure 5**). HfN nanoparticle suspensions exposed to high energy photons (500 nm) display a narrow photoinduced absorption band around 416 nm which only lasts for ≈100 fs with significant intensity (on the order of, or exceeding the intensity of the transient bleach). With 630 nm excitation the phenomenon is not seen, unless the sample has previously been irradiated with 500 nm pulses, or the sample is left stationary instead of moved and exposed to high intensity 630 nm pulses (Figures S16 and S17, Supporting Information). This is accompanied with localized permanent bleaching of the sample, confirming that this is not the missing hot carrier component. The position of the phenomenon with 630 nm excitation red-shifts and is found to be consistently 0.4 ± 0.1 eV above the pump photon energy.
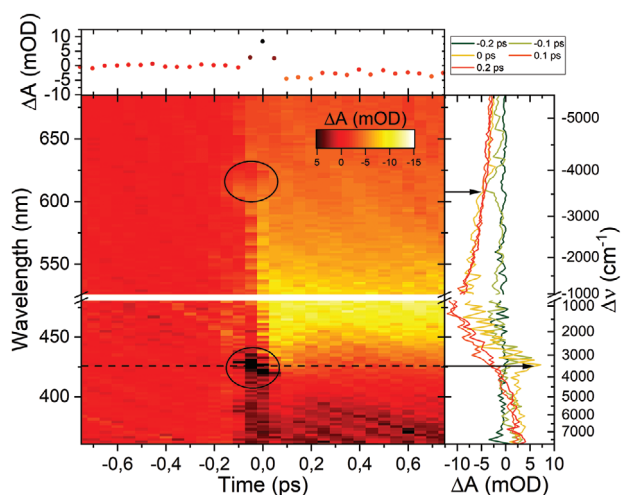
Its presence always follows exposure to either high intensity or high photon energy pulses, and not for irradiation with low intensity and low photon energy pulses. This indicates that the phenomenon is due to some long-lasting change to the HfN nanoparticles and questions their long-term stability under high-demanding operating conditions, but does not explain what is being observed.

There are several coherent Raman phenomena, which could cause a signal in ultrafast TA experiments.[71–73] Given that HfN has a high third-order susceptibility ($\chi^{(3)}$) like other group-4 nitrides,[74,75] it may display nonlinear optical processes including inverse Raman scattering, or stimulated Raman scattering. In the case of stimulated Raman scattering, a loss in transmission (i.e., higher absorbance) blue-shifted from the pump accompanying a gain in transmission (i.e., decrease in absorbance) red-shifted from the pump can be expected.[73] A short-lived photoinduced absorbance blue-shifted from the pump is clearly visible around 416 nm. Scrutinizing 0.4 ± 0.1 eV below the pump photon energy in Figure 5 does give some indication that there may be a weak short-lived decrease in absorbance ≈610 nm. However, as it is followed by a photoinduced bleach of the LSPR developing within the instrumental response time, it is difficult to determine if there is indeed such short-lived stimulated Raman signal, or a slight miscorrection of the experimental chirp.

If this phenomenon is indeed stimulated Raman scattering, then the 0.4 ± 0.1 eV shift would give an indication of the surface termination. As such, it would be more effective to note that the shift is 3500 ± 800 cm^{-1}, which corresponds roughly to both OH and NH vibrations. Combining this with the observation of a permanent bleach with intense and prolonged 630 nm pulsed irradiation suggests that the HfN may be oxidized and forming hydrated oxide/nitride; although further study is needed to confirm the species. This suggests that HfN nanoparticles may not be as chemically stable in high-demanding aqueous conditions as generally advocated and use as a thermoplasmonic source may require surface passivation if both longevity and intense or energetic light is used. Indeed, recently a method for coating TiN nanoparticles with a shell of silicon oxynitride has been presented, which greatly enhanced the thermal stability of the particles up to 900 °C.[43] In our own temperature-dependent ellipsometry measurements, we applied Al$_2$O$_3$ as thin protection layer using a conformal ALD process, which altogether prevented further surface oxidation when heated to 523 K. Furthermore, since Al$_2$O$_3$ is an excellent thermal conductor, the thermo-plasmonic response would remain largely unaffected.

3. Conclusions

The photophysical and -chemical relaxation pathways in water-dispersed HfN nanoparticles have been studied through fs transient absorption spectroscopy, paired with Lumerical FDTD and COMSOL Multiphysics simulations supported by temperature-dependent ellipsometry. The HfN nanoparticles have been compared to Au nanoparticles, which have well-understood photodynamical regimes, demonstrating the differences, and to validate simulation results. The transient absorption data

Figure 5. TA contour plot of the early-time phenomenon observed during excitation at 500 nm with time trace at 416 nm, and spectra at time delays of −0.2–0.2 ps, circles and arrows highlight the regions with ultrafast signals likely caused by stimulated Raman scattering.

**ADVANCED
SCIENCE NEWS**
www.advancedsciencenews.com

**ADVANCED
OPTICAL
MATERIALS**
www.advopticalmat.de

and simulations are in excellent agreement. We unequivocally demonstrate that HfN nanoparticles convert absorbed photons into heat within <100 fs following photoexcitation; no signature of hot carriers is observed. These results bridge the discrepancy between previous theoretical and experimental work, and demonstrate that in HfN nanoparticles for times beyond the ≈100 fs regime after photoexcitation only heat dissipation takes place. This means that while HfN nanoparticles are not good candidates for hot-carrier induced photochemical reactions, they could be ideal for plasmonic photothermal reactions and to help determine the underlying mechanism in plasmonic photochemical reactions. For the application of HfN nanoparticles as a thermo-plasmonic source in aqueous conditions, the formation of a $HfN_xO_yH_z$ surface layer, which likely explains stimulated Raman signals observed here, should be considered and prevented.

4. Experimental Section

General Techniques: Scanning electron microscopy (SEM) was performed on a FEI Verios 460 at 5 kV acceleration voltage and 100 pA beam current. Energy-dispersive X-ray spectrometry (EDS) measurements were performed with an Oxford Instruments device with a beam acceleration voltage of 20 kV and current of 0.8 nA, with particles adhered to a TEM grid (Cu-mesh with formvar/carbon). X-ray diffraction (XRD) patterns were measured with a Bruker D2 Phaser with Cu K_α radiation ($\lambda = 1.5406$ Å). Atomic layer deposition (ALD) of alumina was performed with a previously published procedure at 250 °C,[76] resulting in a thickness of exactly 10.0 nm. All data and images were further processed using Microsoft Excel, Origin 2017, and ImageJ 2.0 software.

HfN Nanoparticle Synthesis: HfN nanoparticles were synthesized according to an adjusted literature method from HfO_2 using Mg_3N_2 at 1000 °C and purified using an acidic work-up.[45,46] In brief, 300 mg HfO_2 nanoparticles (61–80 nm average particle size, US Research Nanomaterials, Inc.) and 432 mg Mg_3N_2 (325 mesh, Sigma Aldrich) were ground together using pestle and mortar for 5 min in a glovebox. The mixture was transferred to an alumina crucible, placed in a quartz tube, and transferred to a tube oven. The tube was flushed with 100 sccm Ar for 10 min. and then kept at 50 sccm during subsequent heating. The oven was ramped to 1000 °C at 25 °C min^{-1}. and kept for 12 h before allowing the oven to cool down to room temperature. The resulting black powder was added to 60 mL distilled water and transferred to a 200 mL beaker. A clear hiss of escaping gas indicated that there was still active Mg_3N_2 powder in the mixture. Then, 75 mL 1 M HCl was added and the beaker was stirred for 1 h. The dark suspension was centrifuged at 3300 rpm for 15 min, after which the nearly colorless supernatant was decanted and discarded. The pellet was dispersed in 13 mL distilled water by use of vortex and sonication, and centrifuged again at 3300 rpm for 15 min. The deeply purple-colored supernatant was carefully collected (product batch #1), and the pellet was once more dispersed in 13 mL distilled water and centrifuged at 3300 rpm for 15 min. The supernatant was collected (product batch #2) and was added to product batch #1; this combined nanoparticle dispersion was used without further purification. The solution typically remained stable for days to weeks before noticeable precipitation occurred.

Gold Nanoparticle Synthesis: Gold nanoparticles were synthesized using the established Turkevich method:[77,78] 50 mL of 38.8×10^{-3} M sodium citrate (Sigma, 99%) was added to 500 mL of boiling 1×10^{-3} M $HAuCl_4$ (Sigma, 99.995%) and allowed to boil for 15 min before being cooled. The yellow $HAuCl_4$ became transparent and then progressed to a deep red color. The particles were diluted in MiliQ water to have an attenuation of approximately 0.3 OD mm^{-1} and used without further treatment. A UV–Vis spectrum of the Au nanoparticle solution is shown in Figure S4b (Supporting Information).

Reactive Sputter Coating of HfN: A Flexture reactive sputter coating system (Polyteknik AS, Denmark) was used to deposit HfN from a pure Hf target in a nitrogen/argon atmosphere (35.3 sccm Ar and 0.7 sccm N_2) on Si substrates. The base pressure was 8×10^{-8} mbar. The target was cleaned for at least 2 min before deposition. The substrate was rotated at 4 rpm during deposition. Radio frequency (RF) magnetron sputtering with 150 W power at a pressure of 2.2×10^{-3} mbar resulted in a typical deposition rate of 8 nm min^{-1}.

Transient Absorption Spectroscopy: Femtosecond transient absorption experiments were performed using a home-built setup. The initial 800 nm pulses (FWHM 35 ± 1 fs) were produced by a Ti:Sapphire amplifier (Coherent Legend) operating at 5 kHz repetition rate. The output was split into two beams using a 90:10 beam splitter. The pump beam was generated by sending the major part of the 800 nm beam into an optical parametric amplifier (Coherent, Opera), producing pulses with tunable center wavelength and a pulse duration of ≈50 fs FWHM. The differential absorbance between pump on and off was obtained by chopping the pump beam at 2.5 kHz. The pump was further attenuated using a neutral density filter. The white light continuum probe was produced through supercontinuum generation by guiding the remaining part of the 800 nm beam through a mechanical delay stage, variable neutral density filter wheel, and focusing into a CaF_2 crystal (Newlight Photonics, 3 mm thickness, 001-cut, uncoated, the crystal was continuously moved to prevent damage). The remaining 800 nm light in the probe beam was removed using two IR neutral density filters. The polarization of the pump and probe were set to 54.7° (magic angle) to avoid anisotropy effects.[79,80] The pump was focused to a spot of ca. 250 μm diameter, significantly larger than the focused probe spot (ca. 100 μm diameter) and it is thus reasonable to assume that we probe a homogeneously photoexcited sample. Detection of the signal was achieved using a 15 cm spectrograph coupled to a 256-pixel diode array detector. Samples were mounted on a stage which constantly moved both horizontally and vertically to prevent irreversible light-induced changes. The time resolution was determined to be 100–150 fs, and the TA signal decay was verified to not be caused by persistent effects. The pump power was kept relatively low (≈4.0×10^{15} photons/(cm^2 pulse), corresponding to ca. 3.2 W cm^{-2}) and confirmed to be in the linear regime. The UV–Vis extinction of the samples was verified to be identical before and after experiments to ensure that no significant permanent bleaching occurred (except in extreme cases when verifying the stimulated Raman scattering signal). Data analysis was performed using Matlab for chirp correction and stretched exponential fitting, and Glotaran[81] for one and two-component exponential fitting. The $t = 0$ ps was defined as when the transient bleach signal is at 50% of its maximum.

Temperature-Dependent Ellipsometry: Temperature-dependent ellipsometry was performed on a J.A. Woollam variable angle spectrometric ellipsometer (VASE) fitted with a copper heating stage. Reported temperatures correspond to the temperature of the heating stage. Samples were allowed to thermally stabilize at each temperature for 20 min. before ellipsometric measurement at 6 different angles (50–75° with 5° intervals). The optical constants for alumina-covered HfN were retrieved using WVASE32 and CompleteEASE software by isolating the HfN optical constants from the alumina contribution. The alumina contribution was individually measured on alumina covered Si from the same ALD batch process.

Optical and Heat Transfer Modeling: A detailed account of the modeling is provided in the Supporting Information. Briefly, Lumerical FDTD was used to determine the optical absorption cross sections of HfN and Au nanoparticles and their 3D absorbed power maps. COMSOL Multiphysics 5.1 was used to solve the heat transfer equations in space and time.

Supporting Information

Supporting Information is available from the Wiley Online Library or from the author.

ADVANCED
SCIENCE NEWS
www.advancedsciencenews.com

ADVANCED
OPTICAL
MATERIALS
www.advopticalmat.de

Conflict of Interest

The authors declare no conflict of interest.

Data Availability Statement

Research data are not shared.

[1] K. A. Willets, R. P. Van Duyne, *Annu. Rev. Phys. Chem.* **2007**, *58*, 267.

[2] K. M. Mayer, J. H. Hafner, *Chem. Rev.* **2011**, *111*, 3828.

[3] N. J. Halas, *Faraday Discuss.* **2019**, *214*, 13.

[4] M. L. Brongersma, N. J. Halas, P. Nordlander, *Nat. Nanotechnol.* **2015**, *10*, 25.

[5] U. Guler, A. Boltasseva, V. M. Shalaev, *Science* **2014**, *344*, 263.

[6] G. V. Naik, V. M. Shalaev, A. Boltasseva, *Adv. Mater.* **2013**, *25*, 3264.

[7] S. J. Kim, I. Thomann, J. Park, J.-H. Kang, A. P. Vasudev, M. L. Brongersma, *Nano Lett.* **2014**, *14*, 1446.

[8] B. Goris, A. De Backer, S. Van Aert, S. Gómez-Graña, L. M. Liz-Marzán, G. Van Tendeloo, S. Bals, *Nano Lett.* **2013**, *13*, 4236.

[9] U. Guler, A. Boltasseva, V. M. Shalaev, *Science* **2014**, *344*, 263.

[10] C. Defilippi, D. V. Shinde, Z. Dang, L. Manna, C. Hardacre, A. J. Greer, C. D'Agostino, C. Giordano, *Angew. Chem., Int. Ed.* **2019**, *58*, 15464.

[11] C. Defilippi, D. V. Shinde, Z. Dang, L. Manna, C. Hardacre, A. J. Greer, C. D'Agostino, C. Giordano, *Angew. Chem.* **2019**, *131*, 15610.

[12] Y. Yuan, J. Wang, S. Adimi, H. Shen, T. Thomas, R. Ma, J. P. Attfield, M. Yang, *Nat. Mater.* **2019**, *18*, 1.

[13] Y. Zhang, S. He, W. Guo, Y. Hu, J. Huang, J. R. Mulcahy, W. D. Wei, *Chem. Rev.* **2018**, *118*, 2927.

[14] G. V. Hartland, L. V. Besteiro, P. Johns, A. O. Govorov, *ACS Energy Lett.* **2017**, *2*, 1641.

[15] G. Baffou, I. Bordacchini, A. Baldi, R. Quidant, *Light: Sci. Appl.* **2020**, *9*, 2047.

[16] L. Mascaretti, A. Naldoni, *J. Appl. Phys.* **2020**, *128*, 041101.

[17] L. R. Khundkar, A. H. Zewail, *Annu. Rev. Phys. Chem.* **1990**, *41*, 15.

[18] E. Traver, R. A. Karaballi, Y. E. Monfared, H. Daurie, G. A. Gagnon, M. Dasog, *ACS Appl. Nano Mater.* **2020**, *3*, 2787.

[19] R. A. Karaballi, Y. Esfahani Monfared, M. Dasog, *Langmuir* **2020**, *36*, 5058.

[20] J. Chen, X. Wang, F. Tang, X. Ye, L. Yang, Y. Zhang, *Results Phys.* **2020**, *16*, 102867.

[21] F. Zhao, X. Xue, W. Fu, Y. Liu, Y. Ling, Z. Zhang, *J. Phys. Chem. C* **2019**, *123*, 29353.

[22] M. Wu, H. Wei, Y. Wei, A. Yao, J. Bu, J. Lin, Z. Dong, Y. Chen, Y. Cui, Z. Wu, *Vib. Spectrosc.* **2018**, *95*, 32.

[23] C. L. Haynes, R. P. Van Duyne, *J. Phys. Chem. B* **2003**, *107*, 7426.

[24] E. C. Le Ru, P. G. Etchegoin, *Chem. Phys. Lett.* **2006**, *423*, 63.

[25] G. Baffou, F. Cichos, R. Quidant, *Nat. Mater.* **2020**, *19*, 946.

[26] D. Mateo, J. L. Cerrillo, S. Durini, J. Gascon, *Chem. Soc. Rev.* **2021**, *50*, 2173.

[27] I. Alessandri, J. R. Lombardi, *Chem. Rev.* **2016**, *116*, 14921.

[28] C. S. Wondergem, J. J. G. Kromwijk, M. Slagter, W. L. Vrijburg, E. J. M. Hensen, M. Monai, C. Vogt, B. M. Weckhuysen, *ChemPhysChem* **2020**, *21*, 625.

[29] Xiaoming Wen, S. Chung, N. Gupta, Hongze Xia, Yu Feng, S. Shrestha, Shujuan Huang, T. W. Kee, T. Harad, G. Conibeer, in *2015 IEEE 42nd Photovoltaic Specialist Conf.*, IEEE, Piscataway, NJ **2015**, pp. 1–4.

[30] S. Chung, X. Wen, S. Huang, N. Gupta, G. Conibeer, S. Shrestha, T. Harada, T. W. Kee, *Sol. Energy Mater. Sol. Cells* **2017**, *169*, 13.

[31] S. Chung, S. Shrestha, X. Wen, Y. Feng, N. Gupta, H. Xia, P. Yu, J. Tang, G. Conibeer, *Sol. Energy Mater. Sol. Cells* **2016**, *144*, 781.

[32] S. Shrestha, S. Chung, Y. Liao, P. Wang, W. Cao, X. Wen, N. Gupta, G. Conibeer, *Jpn. J. Appl. Phys.* **2017**, *56*, 08MA03.

[33] H. Xia, X. Wen, Y. Feng, R. Patterson, S. Chung, N. Gupta, S. Shrestha, G. Conibeer, *Sol. Energy Mater. Sol. Cells* **2016**, *150*, 51.

[34] A. Habib, F. Florio, R. Sundararaman, *J. Opt.* **2018**, *20*, 064001.

[35] R. Sato, S. Ishii, T. Nagao, M. Naito, Y. Takeda, *ACS Photonics* **2018**, *5*, 3452.

[36] H. George, J. Reed, M. Ferdinandus, C. DeVault, A. Lagutchev, A. Urbas, T. B. Norris, V. M. Shalaev, A. Boltasseva, N. Kinsey, *Opt. Mater. Express* **2019**, *9*, 3911.

[37] B. T. Diroll, S. Saha, V. M. Shalaev, A. Boltasseva, R. D. Schaller, *Adv. Opt. Mater.* **2020**, *8*, 2000652.

[38] S. Dal Forno, J. Lischner, *Phys. Rev. Mater.* **2019**, *3*, 115203.

[39] S. H. C. Askes, N. J. Schilder, E. Zoethout, A. Polman, E. C. Garnett, *Nanoscale* **2019**, *11*, 20252.

[40] R. Erwin, *Metall. Mater. Trans. B* **1970**, *1*, 1249.

[41] N. Dahal, V. Chikan, *Inorg. Chem.* **2012**, *51*, 518.

[42] Y. Esfahani Monfared, M. Dasog, *Canadian J. Chem.* **2021**, https://doi.org/10.1139/cjc-2020-0335.

[43] C. Berrospe Rodriguez, A. Alvarez Barragan, G. Nava, S. Exarhos, L. Mangolini, *ACS Appl. Nano Mater.* **2020**, *3*, 4504.

[44] A. Alvarez Barragan, N. V. Ilawe, L. Zhong, B. M. Wong, L. Mangolini, *J. Phys. Chem. C* **2017**, *121*, 2316.

[45] R. A. Karaballi, G. Humagain, B. R. A. Fleischman, M. Dasog, *Angew. Chem., Int. Ed.* **2019**, *58*, 3147.

[46] R. A. Karaballi, G. Humagain, B. R. A. Fleischman, M. Dasog, *Angew. Chem.* **2019**, *131*, 3179.

[47] S. Link, M. A. El-Sayed, *J. Phys. Chem. B* **1999**, *103*, 8410.

[48] M. Hu, X. Wang, G. V Hartland, V. Salgueiriño-Maceira, L. M. Liz-Marzán, *Chem. Phys. Lett.* **2003**, *372*, 767.

[49] M. Hu, G. V. Hartland, *J. Phys. Chem. B* **2002**, *106*, 7029.

[50] S. Hashimoto, D. Werner, T. Uwada, *J. Photochem. Photobiol. C: Photochem. Rev.* **2012**, *13*, 28.

[51] S. Link, A. Furube, M. B. Mohamed, T. Asahi, H. Masuhara, M. A. El-Sayed, *J. Phys. Chem. B* **2002**, *106*, 945.

[52] A. M. Brown, R. Sundararaman, P. Narang, A. M. Schwartzberg, W. A. Goddard, H. A. Atwater, *Phys. Rev. Lett.* **2017**, *118*, 087401.

[53] E. T. Jensen, R. E. Palmer, W. Allison, J. F. Annett, *Phys. Rev. Lett.* **1991**, *66*, 492.

[54] P. B. Allen, *Phys. Rev. Lett.* **1987**, *59*, 1460.

[55] E. F. Westrum, J. A. Sommers, *J. Therm. Anal. Calorim.* **2002**, *69*, 103.

[56] H. O. Pierson, *Handbook of Refractory Carbides and Nitrides: Properties, Characteristics, Processing, and Applications*, William Andrew Inc., Norwich, NY **1996**.

[57] X. J. Chen, V. V. Struzhkin, S. Kung, H. K. Mao, R. J. Hemley, A. N. Christensen, *Phys. Rev. B: Condens. Matter Mater. Phys.* **2004**, *70*, 014501.

[58] M. Chauhan, D. C. Gupta, *Int. J. Refract. Met. Hard Mater.* **2014**, *42*, 77.

[59] W. Spengler, R. Kaiser, A. N. Christensen, G. Müller-Vogt, *Phys. Rev. B* **1978**, *17*, 1095.

[60] Z. Lin, L. V. Zhigilei, V. Celli, *Phys. Rev. B: Condens. Matter Mater. Phys.* **2008**, *77*, 075133.

[61] P. H. M. Böttger, E. Lewin, J. Patscheider, V. Shklover, D. G. Cahill, R. Ghisleni, M. Sobiech, *Thin Solid Films* **2013**, *549*, 232.

[62] J. Alper, K. Hamad-Schifferli, *Langmuir* **2010**, *26*, 3786.

[63] G. V. Hartland, *Phys. Chem. Chem. Phys.* **2004**, *6*, 5263.

[64] J. A. Briggs, G. V. Naik, Y. Zhao, T. A. Petach, K. Sahasrabuddhe, D. Goldhaber-Gordon, N. A. Melosh, J. A. Dionne, *Appl. Phys. Lett.* **2017**, *110*, 101901.

[65] H. Reddy, U. Guler, Z. Kudyshev, A. V. Kildishev, V. M. Shalaev, A. Boltasseva, *ACS Photonics* **2017**, *4*, 1413.

[66] P. Mulvaney, *Langmuir* **1996**, *12*, 788.

[67] B. Saha, J. Acharya, T. D. Sands, U. V. Waghmare, *J. Appl. Phys.* **2010**, *107*, 033715.

[68] L. Zhou, C. Zhang, M. J. McClain, A. Manjavacas, C. M. Krauter, S. Tian, F. Berg, H. O. Everitt, E. A. Carter, P. Nordlander, N. J. Halas, *Nano Lett.* **2016**, *16*, 1478.

[69] G. Tagliabue, J. S. DuChene, M. Abdellah, A. Habib, D. J. Gosztola, Y. Hattori, W.-H. Cheng, K. Zheng, S. E. Canton, R. Sundararaman, J. Sá, H. A. Atwater, *Nature Materials* **2020**, *19*, 1312.

[70] P. Patsalas, N. Kalfagiannis, S. Kassavetis, G. Abadias, D. V. Bellas, C. Lekka, E. Lidorikis, *Mater. Sci. Eng., R* **2018**, *123*, 1.

[71] E. Ploetz, S. Laimgruber, S. Berner, W. Zinth, P. Gilch, *Appl. Phys. B* **2007**, *87*, 389.

[72] S. Umapathy, A. Lakshmanna, B. Mallick, *J. Raman Spectrosc.* **2009**, *40*, 235.

[73] U. Harbola, S. Umapathy, S. Mukamel, *Phys. Rev. A* **2013**, *88*, 011801(R).

[74] S. S. Kharintsev, A. V. Kharitonov, S. K. Saikin, A. M. Alekseev, S. G. Kazarian, *Nano Lett.* **2017**, *17*, 5533.

[75] N. Kinsey, A. A. Syed, D. Courtwright, C. DeVault, C. E. Bonner, V. I. Gavrilenko, V. M. Shalaev, D. J. Hagan, E. W. Van Stryland, A. Boltasseva, *Opt. Mater. Express* **2015**, *5*, 2395.

[76] E. Kontoleta, A. Tsoukala, S. H. C. Askes, E. Zoethout, E. Oksenberg, H. Agrawal, E. C. Garnett, *ACS Appl. Mater. Interfaces* **2020**, *12*, 35986.

[77] J. Turkevich, P. C. Stevenson, J. Hillier, *Discuss. Faraday Soc.* **1951**, *11*, 55.

[78] J. Kimling, M. Maier, B. Okenve, V. Kotaidis, H. Ballot, A. Plech, *J. Phys. Chem. B* **2006**, *110*, 15700.

[79] H. E. Lessing, A. von Jena, *Chem. Phys. Lett.* **1977**, *46*, 111.

[80] S. Schott, A. Steinbacher, J. Buback, P. Nuernberger, T. Brixner, *J. Phys. B: At., Mol. Opt. Phys.* **2014**, *47*, 124014.

[81] J. J. Snellenburg, S. P. Laptenok, R. Seger, K. M. Mullen, I. H. M. van Stokkum, *J. Stat. Software* **2012**, *49*, https://doi.org/10.18637/jss.v049.i03.

2100510 (11 of 11)